



The link among X-ray spectral properties, AGN structure, and the host galaxy

G. Mountrichas¹, A. Viitanen^{2,1,3}, F. J. Carrera¹, H. Stiele^{4,5}, A. Ruiz⁶, I. Georgantopoulos⁶,
S. Mateos¹, and A. Corral¹

¹ Instituto de Física de Cantabria (CSIC-Universidad de Cantabria), Avenida de los Castros, 39005 Santander, Spain
e-mail: gmountrichas@gmail.com

² INAF – Osservatorio Astronomico di Roma, Via Frascati 33, 00040 Monteporzio Catone, Italy

³ Department of Physics, University of Helsinki, PO Box 64, 00014 Helsinki, Finland

⁴ Jülich Supercomputing Centre, Forschungszentrum Jülich, Wilhelm-Johnen-Straße, 52428 Jülich, Germany

⁵ Institute of Astronomy, National Tsing Hua University, No. 101 Sect. 2 Kuang-Fu Road, 30013 Hsinchu, Taiwan

⁶ National Observatory of Athens, Institute for Astronomy, Astrophysics, Space Applications and Remote Sensing, Ioannou Metaxa and Vasileos Pavlou, 15236 Athens, Greece

Received 9 October 2023 / Accepted 27 December 2023

ABSTRACT

In this work, we compare the supermassive black hole (SMBH) and host galaxy properties of X-ray obscured and unobscured AGN. For that purpose, we used ~35 000 X-ray detected AGN in the 4XMM-DR11 catalogue for which there are available measurements for their X-ray spectral parameters, such as the hydrogen column density, N_{H} , and photon index, Γ , from the XMM2Athena Horizon 2020 European project. We constructed the spectral energy distributions (SEDs) of the sources, and we calculated the host galaxy properties via SED fitting analysis, utilising the CIGALE code. We applied strict photometric requirements and quality selection criteria to include only sources with robust X-ray and SED fitting measurements. Our sample consists of 1443 AGN. In the first part of our analysis, we used different N_{H} thresholds (10^{23} cm^{-2} or 10^{22} cm^{-2}) while also taking into account the uncertainties associated with the N_{H} measurements in order to classify these sources as obscured and unobscured (or mildly obscured). We find that obscured AGN tend to live in more massive systems (by ~0.1 dex) that have a lower star-formation rate, SFR, (by ~0.25 dex) compared to their unobscured counterparts. However, only the difference in stellar mass, M_* , appears statistically significant ($>2\sigma$). The results do not depend on the N_{H} threshold used to classify AGN. The differences in M_* and SFR are not statistically significant for luminous AGN ($\log(L_{\text{X},2-10 \text{ KeV}}/\text{erg s}^{-1}) > 44$). Our findings also show that unobscured AGN have, on average, higher specific black hole accretion rates, λ_{SMBHAR} , compared to their obscured counterparts, a parameter which is often used as a proxy of the Eddington ratio. In the second part of our analysis, we cross-matched the 1443 X-ray AGN with the SDSS DR16 quasar catalogue of Wu and Shen to obtain information on the SMBH properties of our sources. This resulted in 271 type 1 AGN at $z < 1.9$. Our findings show that type 1 AGN with increased N_{H} ($>10^{22} \text{ cm}^{-2}$) tend to have higher black hole masses, M_{BH} , compared to AGN with lower N_{H} values at similar M_* . The M_{BH}/M_* ratio remains consistent for N_{H} values below 10^{22} cm^{-2} , but it exhibits signs of increasing at higher N_{H} values. Finally, we detected a correlation between Γ and Eddington ratios, but only for type 1 sources with $N_{\text{H}} < 10^{22} \text{ cm}^{-2}$.

Key words. methods: observational – galaxies: active – galaxies: evolution – galaxies: statistics – X-rays: galaxies – X-rays: general

1. Introduction

Active galactic nuclei (AGN) are powered by accretion onto the supermassive black hole (SMBH) that is located in the centre of most, if not all, galaxies. It is well known that AGN and their host galaxies co-evolve. This coeval growth is manifested in a number of ways. For instance, strong correlations have been found between the mass of the SMBH, M_{BH} , and various galaxy properties, such as the bulge, or stellar mass (M_*), and the stellar velocity dispersion of galaxies (e.g. Magorrian et al. 1998; Ferrarese & Merritt 2000; Häring & Rix 2004). Moreover, both the AGN activity and the star formation are fed by the same material (cold gas) and peak at similar cosmic times ($z \sim 2$; e.g. Boyle et al. 2000; Sobral et al. 2013). Thus, for the purposes of understanding galaxy evolution, it is important to shed light on the structure of AGN in order to elucidate the physical mechanism(s) that feed the central SMBH and to study the AGN feedback.

One important aspect of this pursuit is to decipher the physical difference between obscured and unobscured AGN.

According to the unification model (e.g. Urry & Padovani 1995; Nenkova et al. 2002; Netzer 2015), AGN are surrounded by a dusty gas torus structure that absorbs radiation emitted from the SMBH and the accretion disc around it. This absorbed radiation is then re-emitted at longer (infrared) wavelengths. In the context of this model, an AGN is classified as obscured or unobscured depending on the inclination of the line of sight with respect to the symmetry axis of the accretion disc and torus. When the AGN is observed edge-on, the source is characterised as obscured, while it is classified as unobscured when the AGN is viewed face-on. Recent investigations have proposed a more intricate structure for AGN to account for the diverse classifications observed at different wavelengths, such as X-ray versus optical classifications (e.g. Ogawa et al. 2021; Esparza-Arredondo et al. 2021). Advanced techniques such as infrared interferometry have enabled detailed examination of the inner regions of AGN, unveiling complexities within the torus and challenging the conventional notion of a simple, smooth toroidal model (e.g. Tristram et al. 2007). Studies focusing on short timescale variability in X-ray column density have

identified fluctuations, indicating dynamic changes in the distribution of obscuring material (e.g. [Marinucci et al. 2016](#)). While the presence of clumps in the torus contributes to the diversity of observed AGN types and offers valuable insights into the accretion processes around SMBHs, according to the unification model, the inclination angle remains the pivotal factor for distinguishing between obscured and unobscured AGN.

An alternative interpretation of the AGN obscuration comes from the class of the evolutionary models. In this case, the different AGN types are attributed to SMBH and their host galaxies being observed at different phases. The main idea of these models is that obscured AGN are observed at an early phase, when the energetic output from the accretion disc around the SMBH is not strong enough and incapable of expelling the gas that surrounds it. As material is accreted onto the SMBH, its energetic output becomes more powerful and eventually pushes away the obscuring material (e.g. [Ciotti & Ostriker 1997](#); [Hopkins et al. 2006](#); [Somerville et al. 2008](#)).

Studying the two AGN populations can shed light on many different aspects of the AGN-galaxy interplay. An important step towards this direction is to first understand the nature of obscured and unobscured AGN. A popular approach to uncover their features and behaviours is to compare the host galaxy properties of the two AGN types. If the different AGN populations live in similar environments, this would provide support to the unification model, whereas if they reside in galaxies of different properties, it would suggest that they are observed at different evolutionary phases.

Previous studies that compared the host galaxy properties of obscured and unobscured AGN found conflicting results, depending on the wavelengths used to identify AGN (optical, infrared, X-rays) and the obscuration criteria applied to classify sources. For X-ray-selected AGN, when the source classification is based on optical criteria, for instance, using optical spectra to identify broad and narrow emission lines, most studies have found that obscured AGN (type 2) tend to live in more massive galaxies compared to their unobscured (type 1) counterparts. However, both AGN types live in systems with similar levels of star formation (e.g. [Zou et al. 2019](#); [Mountrichas et al. 2021a](#)). When the classification is based on X-ray criteria, though, for instance on the value of the hydrogen column density, N_H , some studies have not observed significant differences in the host galaxy properties of obscured and unobscured AGN (e.g. [Masoura et al. 2021](#); [Mountrichas et al. 2021c](#)), while other studies have found an increase of M_* with N_H ([Lanzuisi et al. 2017](#)). Differences regarding both the M_* and the stellar populations of the two AGN classes have also been reported ([Georgantopoulos et al. 2023](#)).

Another important aspect that can shed light on the structure of AGN is the study of the possible correlation between the X-ray spectral index, Γ , and the Eddington ratio, n_{Edd} . The Eddington ratio is defined as the ratio of the AGN bolometric luminosity, L_{bol} , and the Eddington luminosity, L_{Edd} ($L_{\text{Edd}} = 1.26 \times 10^{38} M_{\text{BH}}/M_{\odot} \text{ erg s}^{-1}$, where M_{BH} is the mass of the SMBH). The relation between Γ and n_{Edd} has been interpreted as the link between the accretion efficiency in the accretion disc and the physical status of the corona. Due to the larger amount of optical and UV photons produced by the accretion disc, the X-ray emitting plasma is more efficiently cooled at a higher n_{Edd} (e.g. [Vasudevan & Fabian 2007](#); [Davis & Laor 2011](#)). Alternatively, a correlation between Γ and n_{Edd} could be explained by the significant dependence of the cut-off energy on the n_{Edd} (for more details see [Ricci et al. 2018](#)). Apart from the physical interpretation of a possible correla-

tion between Γ and n_{Edd} , it is still not clear whether such a correlation is robust or universal, since relevant studies have found conflicting results (e.g. [Shemmer et al. 2008](#); [Risaliti et al. 2009](#); [Sobolewska & Papadakis 2009](#); [Brightman et al. 2013](#); [Trakhtenbrot et al. 2017](#); [Kamraj et al. 2022](#)).

In this work, we utilised X-ray AGN from the 4XMM-DR11 catalogue, for which there are available measurements for their X-ray spectral parameters, within the framework of the XMM2Athena¹ project. The 4XMM-DR11 dataset proved advantageous for our investigations due to its extensive collection of X-ray sources detected by the *XMM-Newton* observatory. The utilisation of *XMM-Newton* is particularly beneficial due to its high sensitivity and spatial resolution, allowing for the identification of faint and distant sources. Furthermore, the dataset demonstrates homogeneity, as the processed data within it adhere to a consistent processing methodology. Using the calculations for the spectral parameters, we classified sources into X-ray obscured and unobscured and compared their host galaxy properties. We then cross-matched the X-ray dataset with the [Wu & Shen \(2022\)](#) catalogue, which provides calculations for SMBH properties, such as black hole mass, M_{BH} , and bolometric luminosity, L_{bol} , for SDSS quasars. This enabled us to compare the SMBH properties of the two AGN populations.

The paper is structured as follows. In Sect. 2, the two aforementioned catalogues are described. Section 3 presents the spectral energy distribution (SED) fitting analysis followed to measure the host galaxy properties. The selection criteria and the final samples are described in Sect. 4. Our results and conclusions are presented in Sect. 5. In Sect. 6, we summarise the main findings of this work.

2. Data

In this work, we used X-ray AGN included in the 4XMM-DR11 catalogue ([Webb et al. 2020](#)). The 4XMM-DR11 is the fourth generation catalogue of serendipitous X-ray sources from the European Space Agency's (ESA) *XMM-Newton* observatory. It has been created by the *XMM-Newton* Survey Science Centre (SSC) on behalf of ESA. The catalogue contains 319 565 detections with spectra in 11 907 observations. There are 100 237 (31.4%) detections that were made in both detectors, 135 342 (45.5%) detections that come solely from the pn detector, and 73 986 (23.2%) detections that are only from the MOS cameras.

There are 210 444 sources that have available spectrum from one or more detections. The process followed for the classification and fitting of these sources has been done within the framework of the XMM2Athena project and is described in detail in Viitanen et al. (in prep.). In brief, the [Tranin et al. \(2022\)](#) catalogue was used to classify the sources. In [Tranin et al. \(2022\)](#), they used a reference sample constructed by cross-matching the *Swift*-XRT (2SXPS; [Evans et al. 2020](#)) sample and the tenth data release of the *XMM-Newton* serendipitous dataset (4XMM-DR10) with catalogues of identified AGN, stars, and other X-ray source types (for more details, see their Table 2 and Sect. 2.1.2). The 210 444 sources were cross-matched with the [Tranin et al. \(2022\)](#) catalogue using a matching radius of 1". The final number of sources with available classification is 92 238. Out of them, 76 610 are AGN, 14 308 are stars, 1091 are X-ray binaries (XRBs), and 229 are cataclysmic variables (CVs).

For the X-ray sources classified as AGN, we calculated photometric redshifts for those with a reliable optical counterpart in SDSS or PanSTARRS following the methodology pre-

¹ <http://xmm-ssc.irap.omp.eu/xmm2athena/>

sented in Ruiz et al. (2018). In the case of SDSS sources with spectroscopic observations, the corresponding redshift was used instead. There are 35 538 AGN with available redshift (8467 of them have spectroscopic redshift). A detailed presentation of this photometric redshift catalogue is presented in Ruiz et al. (in prep.).

The X-ray spectral analysis of these AGN was conducted within the framework of the XMM2Athena project (Webb et al. 2023). Details of this analysis can be found in Viitanen et al. (in prep.). In summary, a Bayesian spectral fit is performed with the BXA tool (Buchner et al. 2014) that facilitates the connection between XSPEC, which is used for the analysis of the X-ray spectral data (Arnaud 1996), and the nested sampling package UltraNest (Buchner et al. 2021). An uninformative prior was assigned to each parameter within the model, and the exploration of the entire parameter space with equal-weighted sampling points was carried out using the MLFriends algorithm (Buchner 2019), implemented within UltraNest. UltraNest is a Bayesian inference library designed for high-dimensional parameter estimation and model selection. UltraNest employs a nested sampling algorithm that works by enclosing high likelihood regions within a set of nested iso-likelihood contours. The algorithm then successively samples from the prior within these contours, effectively exploring the parameter space in a way that efficiently allocates computational resources to regions of higher likelihood. This makes nested sampling particularly effective for problems with multiple modes, as it naturally discovers and characterises these modes. As part of the fitting process, the empirical background model in the BXA.SHERPA.BACKGROUND module was utilised. This model has two parts. One part models the detector background and contains the contribution of lines and is not folded through the instrumental response. The second part accounts for emission of the cosmic X-ray background and X-ray emission of the local hot bubble and Galactic halo. The background model, which is made up of a mixture of power laws, Gaussian lines, and thermal emission components, is fitted in a multi-step process to the background spectrum with the model increasing in complexity in each step and with the parameters of the previous steps constrained within a narrow range of the best-fit value obtained in the previous step. A χ^2 test was used to estimate the goodness of fit of the background spectra, and p -values were then obtained based on the χ^2 values and the number of effective parameters.

For the fitting of the source X-ray spectrum, a power law with two absorbing media was used: the local Galactic absorption with the column density fixed to the total column density in that line of sight plus in situ absorption at the AGN redshift with a free column density. For the free parameters of the model, the following priors were applied: $\log f_X \in [-17, -7]$ ($\text{erg s}^{-1} \text{cm}^{-2}$); $\Gamma \in [0, 6]$, $\log \text{NH} \in [20, 26]$ (cm^{-2}); and IIN (normalisation) $\in [0, 5]$, where f_X and IIN are the X-ray flux and the inter-instrument normalisation (in the case of PN and MOS detections). To quantify the goodness of fit, a p -value is provided in the catalogue. Its calculation is described in detail in Viitanen et al. (in prep.). For each free parameter the catalogue includes the median and mode values, the 5 and 95 percentiles as well as the values that encompass the narrowest 90% interval (taken as the uncertainty of the mode). The parameters used in our analysis are the mode values of N_{H} , Γ , and the fluxes (calculated in the 2–10 keV energy band). Using these estimated parameters, the X-ray luminosities, L_X , were calculated after correcting for the fitted intrinsic absorption. We opted for mode values because they are the most probable values of the distribution, and they capture the cases that are closer to the

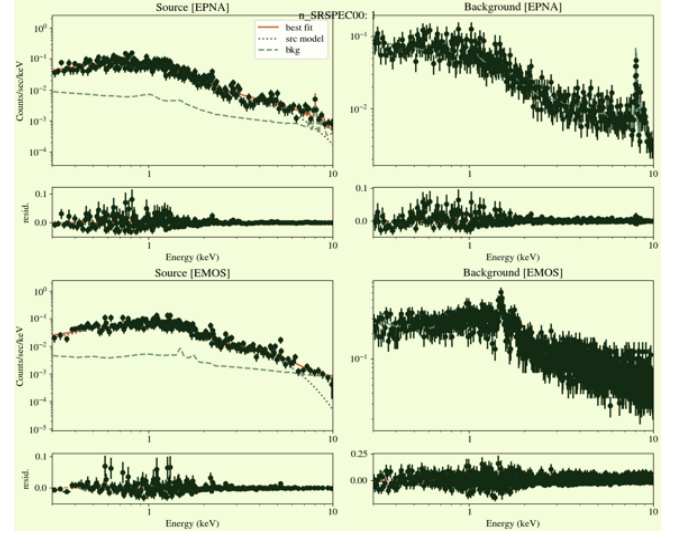


Fig. 1. Example of a source spectrum and model fit (left panels), including the background modelling (right panels) for the PN (top panels) and MOS (bottom panels).

edges of the sampled interval better than the median values. It is important to highlight that this selection, however, does not impact the overall results and conclusions of our study. An example of a source spectrum and model fit including the background modelling is presented in Fig. 1.

One goal of this study is to compare the SMBH properties of X-ray obscured and unobscured AGN. To add this information to our sources, we cross-matched the 35 538 AGN with the Wu & Shen (2022) catalogue. This catalogue includes the continuum and emission line properties for 750 414 broad-line quasars from the data release 16 of SDSS (DR16Q) measured through optical spectroscopy. The quasars span a range of $0.1 \leq z \leq 6$ and $44 \leq \log(L_{\text{bol}}/\text{erg s}^{-1}) \leq 48$, and the L_{bol} were calculated using the measured continuum luminosity at rest-frame wavelengths of 5100 Å, 3000 Å and 1350 Å, depending on the redshift of the source (for more details see Sect. 4.1 in Wu & Shen 2022). The catalogue also includes single-epoch virial M_{BH} . The M_{BH} have been calculated adopting the fiducial recipes on H β (for sources with $z < 0.7$) or the Mg II (for sources with $0.7 \leq z < 1.9$) lines. At higher redshifts, the C IV line was measured. These M_{BH} and L_{bol} were used to calculate the n_{Edd} .

The default redshifts in DR16Q are mostly based on the redshifts derived by the SDSS pipeline (Bolton et al. 2012). Lyke et al. (2020) also visually inspected a small fraction of quasars and updated their default redshift in DR16Q with visual redshifts. In the catalogue provided by Wu & Shen (2022), they presented improved systemic redshifts using the measured line peaks and correcting for velocity shifts of various lines with respect to the systemic velocity (for more details, see their Sect. 4.2).

3. Calculation of the host galaxy properties

For the calculation of the star-formation rate, SFR, and stellar mass, M_* , of the AGN host galaxies, we applied SED fitting using the CIGALE algorithm (Boquien et al. 2019; Yang et al. 2020, 2022). CIGALE allows for the inclusion of the X-ray flux in the fitting process and has the ability to account for the extinction of the UV and optical emission in the poles of AGN (Yang et al. 2020; Mountrichas et al. 2021b,a; Buat et al. 2021).

Table 1. Models and the values for their free parameters used by CIGALE for the SED fitting.

Parameter	Model/values
Star formation history: delayed model and recent burst	
Age of the main population	1000, 2000, 3000, 4000, 5000, 7000, 10 000, 12 000 Myr
e-folding time	300, 1000, 3000, 7000, 10 000 Myr
Age of the burst	50 Myr
Burst stellar mass fraction	0.0, 0.005, 0.01, 0.015, 0.02, 0.05, 0.10, 0.15
Simple stellar population: Bruzual & Charlot (2003)	
Initial mass function	Chabrier (2003)
Metallicity	0.02 (Solar)
Galactic dust extinction	
Dust attenuation law	Charlot & Fall (2000) law
V-band attenuation A_V	0.2, 0.3, 0.4, 0.5, 0.6, 0.7, 0.8, 0.9, 1, 1.5, 2, 2.5, 3, 3.5, 4
Galactic dust emission: Dale et al. (2014)	
α slope in $dM_{\text{dust}} \propto U^{-\alpha} dU$	2.0
AGN module: SKIRTOR	
Torus optical depth at 9.7 microns $\tau_{9.7}$	3.0, 7.0
Torus density radial parameter p ($\rho \propto r^{-p} e^{-q \cos(\theta) }$)	1.0
Torus density angular parameter q ($\rho \propto r^{-p} e^{-q \cos(\theta) }$)	1.0
Angle between the equatorial plan and edge of the torus	40°
Ratio of the maximum to minimum radii of the torus	20
Viewing angle	30° (type 1), 70° (type 2)
AGN fraction	0.0, 0.1, 0.2, 0.3, 0.4, 0.5, 0.6, 0.7, 0.8, 0.9, 0.99
Extinction law of polar dust	SMC
$E(B - V)$ of polar dust	0.0, 0.2, 0.4
Temperature of polar dust (K)	100
Emissivity of polar dust	1.6
X-ray module	
AGN photon index Γ	1.8
Maximum deviation from the $\alpha_{\text{ox}} - L_{2500\text{\AA}}$ relation	0.2
LMXB photon index	1.56
HMXB photon index	2.0

Notes. For the definition of the various parameter, see Sect. 3.

We used the same templates and parametric grid in the SED fitting process as those used in recent works ([Mountrichas et al. 2021c, 2022c,a, 2023](#); [Mountrichas & Shankar 2023](#)). In brief, the galaxy component was modelled using a delayed star-formation history, SFH, model with a function form $\text{SFR} \propto t \times \exp(-t/\tau)$. A star formation burst was included ([Malek et al. 2018](#); [Buat et al. 2019](#)) as a constant ongoing period of star formation of 50 Myr. Stellar emission was modelled using the single stellar population templates of [Bruzual & Charlot \(2003\)](#) and was attenuated following the [Charlot & Fall \(2000\)](#) attenuation law. To model the nebular emission, CIGALE adopts the nebular templates based on [Villa-Velez et al. \(2021\)](#). The emission of the dust heated by stars was modelled based on [Dale et al. \(2014\)](#), without any AGN contribution. The AGN emission was included using the SKIRTOR models of [Stalevski et al. \(2012, 2016\)](#). CIGALE has the ability to model the X-ray emission of galaxies. In the SED fitting process, the intrinsic L_X in the 2–10 keV band were used. The parameter space used in the SED fitting process is shown in Table 1.

4. Selection criteria and final samples

From the 35 538 AGN available in our catalogue, we used those with flag = 0, provided by the catalogue produced by the XMM2Athena. A detailed description of the flag numbering is given in Viitanen et al. (in prep.). In brief, sources

with flag = 0 have background and source fits with a p -value > 0.01, which is the threshold used to classify a fit as acceptable. There were 29 509 AGN that met this criterion. In our analysis, we needed reliable estimates of the host galaxy properties via SED fitting measurements. Therefore, we required all our X-ray AGN to have available photometry from SDSS or Pan-STARRS, 2MASS, and WISE in the following bands: (u), g , r , i , z , (y), J , H , K , $W1$, $W2$, and $W4$ (e.g. [Mountrichas et al. 2021a,c, 2022c,a](#); [Buat et al. 2021](#)). There were 2,501 AGN that fulfilled these requirements. We note that, although we did not require it, all of these AGN also have $W3$ measurements available. For these sources, we applied an SED fitting using the templates and parameter space described in Sect. 3.

To restrict our analysis of sources to those with the most reliable host galaxy measurements, we excluded badly fitted SEDs. For that purpose, we considered only sources for which the reduced χ^2 , $\chi_r^2 < 5$. This value has been used in previous studies (e.g. [Masoura et al. 2018](#); [Buat et al. 2021](#); [Mountrichas et al. 2022c,a](#); [Koutoulidis et al. 2022](#); [Pouliasis et al. 2022](#)) and is based on visual inspection of the SEDs. This requirement was met by 78% of the sources. To further exclude systems with unreliable measurements of the host galaxy properties, we applied the same method presented in previous studies (e.g. [Mountrichas et al. 2021c,a, 2023](#); [Buat et al. 2021](#); [Koutoulidis et al. 2022](#)). This method is based on a comparison between the value of the best model and the

likelihood-weighted mean value calculated by CIGALE. Specifically in our analysis, we only considered sources with $\frac{1}{5} \leq \frac{\text{SFR}_{\text{best}}}{\text{SFR}_{\text{bayes}}} \leq 5$ and $\frac{1}{5} \leq \frac{M_{*,\text{best}}}{M_{*,\text{bayes}}} \leq 5$, where SFR_{best} and $M_{*,\text{best}}$ are the best-fit values of SFR and M_* , respectively, and $\text{SFR}_{\text{bayes}}$ and $M_{*,\text{bayes}}$ are the Bayesian values estimated by CIGALE. The SFR and M_* criteria were met by 88% and 97% of the sources. Previous studies have employed these ranges for the selection of reliable SFR and M_* estimations while leveraging the CIGALE code (e.g. Mountrichas et al. 2021a,c, 2022c,a,b, 2023; Mountrichas & Shankar 2023; Buat et al. 2021; Koutoulidis et al. 2022; Poulidas et al. 2022). Mountrichas et al. (2021c) explored variations in the range, considering 0.1–0.33 for the lower limit and 3–10 for the upper limit. They affirmed that the outcomes remained insensitive to the specific choice of these limits. In our study, we validate this observation by investigating the impact of varying these boundaries within the specified limits. Our findings indicate that such variations result in a dataset size change of less than 5%, underscoring that they do not introduce significant alterations to our overall results and conclusions.

We also restricted the sample used in our analysis to sources with $z < 1.9$. The reason is twofold: our dataset does not include obscured sources at higher redshifts, and M_{BH} measurements available in the Wu & Shen (2022) catalogue are not reliable at $z > 1.9$ (i.e. M_{BH} calculated using the C IV broad line are considered less reliable). Finally, we excluded sources for which their redshift in the XMM dataset differs more than 0.1 compared to the redshift quoted in the Wu & Shen (2022) catalogue (16 AGN were excluded from this criterion). This threshold was determined by considering that during the process of SED fitting, redshift values are rounded to the nearest tenth decimal place. We note that no filtering has been applied regarding the uncertainties associated with the photometric redshifts available in our catalogue. The vast majority of sources with erroneous photometric redshifts would result in poor SED fits and consequently be excluded by the SED quality criteria previously described. Furthermore, we conducted an investigation to determine whether our results were impacted when restricting the analysis solely to AGN with spectroscopic redshifts, which is discussed in the following section.

There were 1443 X-ray AGN that fulfilled these criteria. Of these sources, 1231 lie at $z < 0.7$ and 212 at $0.7 \leq z < 1.9$. This sample was used in the analysis presented in Sects. 5.1 and 5.2. Of the 1443 AGN, 344 are also included in the Wu & Shen (2022) catalogue. Out of them, 271 are at $z < 1.9$. These 271 AGN were used in our analysis presented in Sect. 5.3.

5. Results and discussion

In this section, we compare the properties of host galaxies (SFR, M_*) and SMBHs (n_{Edd}) X-ray obscured and unobscured AGN. We also study the $L_{\text{bol}}-M_{\text{BH}}$ and $M_{\text{BH}}-M_*$ relations as a function of X-ray obscuration (N_{H}). Finally, we investigate the relation between the powerlaw slope (Γ) of the X-ray spectral model with n_{Edd} .

5.1. Host galaxy properties of X-ray obscured and unobscured active galactic nuclei

In our analysis, we used the 1443 AGN that met the criteria described in Sect. 4. Their distribution in the L_X -redshift plane is presented in Fig. 2. We first split the sources into X-ray obscured and unobscured (or mildly obscured) AGN using

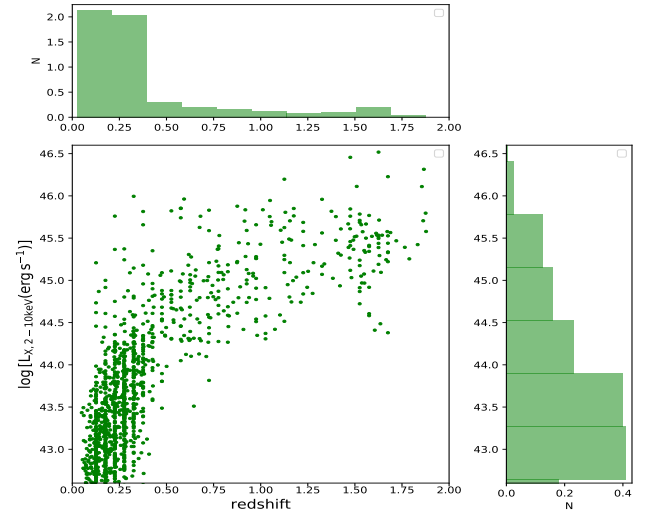


Fig. 2. Distribution of the 1443 X-ray AGN in the L_X -redshift plane.

Table 2. Weighted median values of SFR, M_* , and λ_{SBHAR} for obscured and unobscured AGN.

	$N_{\text{H}} = 10^{23} \text{ cm}^{-2}$		$N_{\text{H}} = 10^{22} \text{ cm}^{-2}$	
	Unobscured	Obscured	Unobscured	Obscured
Number of AGN	1115	34	965	130
$\log \text{SFR}$	0.82	0.57	0.93	0.67
p -value (SFR)	0.10		0.26	
$\log M_*$	10.86	10.95	10.85	10.97
p -value (M_*)	0.02		0.007	
$\log \lambda_{\text{SBHAR}}$	-1.60	-1.71	-1.52	-1.73
p -value (λ_{SBHAR})	0.00006		0.0003	

Notes. We used different N_{H} thresholds for the source classification. The number of sources and the p -values yielded by applying KS tests are also presented.

an N_{H} limit of 10^{23} cm^{-2} . Specifically, we used the lower and upper limits of the 90% confidence interval on the N_{H} mode from the spectral fitting analysis. An AGN was classified as obscured if the lower limit of their N_{H} value was higher than 10^{23} cm^{-2} . Similarly, an AGN was identified as unobscured (or moderately obscured) if the upper limit of its N_{H} value was lower than 10^{23} cm^{-2} . Table 2 presents the number of sources classified. Then, we compared the SFR and M_* of the host galaxies of the two AGN populations. The selection of classification criteria served a dual purpose. Firstly, it relied on recent research findings (Georgantopoulos et al. 2023) that highlight that distinctions in the properties of SMBHs and their host galaxies between obscured and unobscured AGN tend to diminish when the N_{H} value falls below the threshold of $N_{\text{H}} < 23 \text{ cm}^{-2}$. Secondly, by taking into account the uncertainties associated with N_{H} , the classification ensured that only firmly obscured and unobscured sources were categorised as such, enhancing the reliability of the classification process.

The results are presented in Fig. 3. In the figure, we have restricted both datasets to $z < 0.7$. This is because there are no AGN classified as obscured using the criteria described above, at $z > 0.7$, in our dataset. We also note that the distributions have been weighted to account for the different L_X and redshift of obscured and unobscured AGN. For that purpose, each source was assigned a weight based on its L_X and

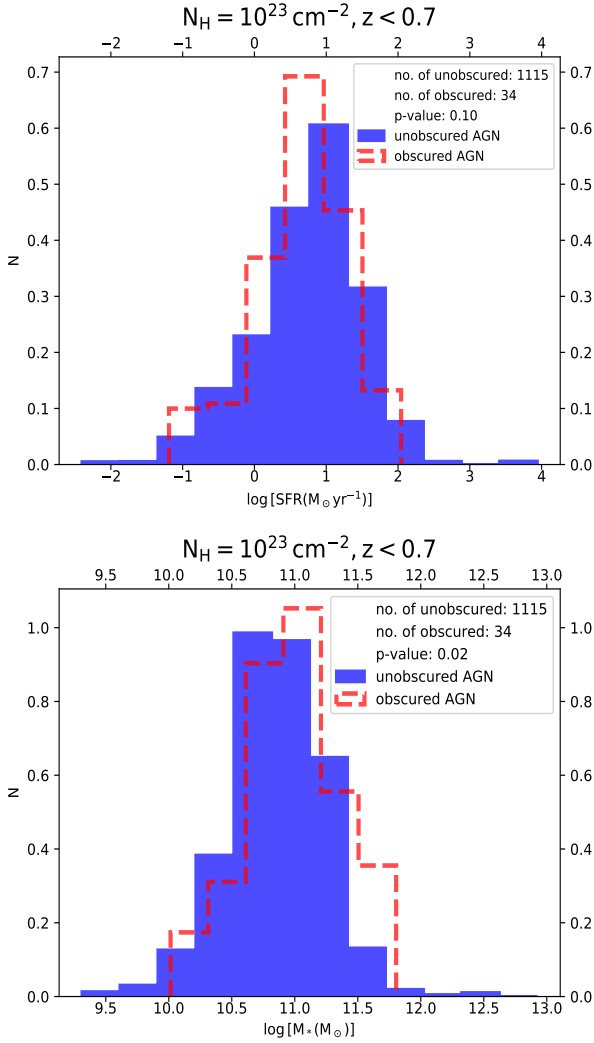


Fig. 3. Host galaxy properties of X-ray obscured (red dashed line histograms) and unobscured AGN (blue shaded histograms). Sources are classified as obscured when the lower limit of their N_H value is higher than 10^{23} cm^{-2} . We classified AGN as unobscured if the upper limit of their N_H value is below 10^{23} cm^{-2} . The top panel presents the SFR distributions of the two AGN populations. The bottom panel shows their M_* distributions. The number of sources and the p -values obtained by applying a KS test are shown in the legend of the plots. Distributions are weighted based on the redshift and L_X of the sources.

redshift following the procedure described in Mountrichas et al. (2019, 2021c, 2022b), Masoura et al. (2021), Buat et al. (2021), Koutoulidis et al. (2022). Specifically, the weight was calculated by measuring the joint L_X distributions of the two populations (i.e. we added the number of obscured and unobscured AGN in each L_X bin in bins of 0.1 dex) and then normalising the L_X distributions by the total number of sources in each bin. The same procedure was followed for the redshift distributions. The total weight that was assigned in each source was the product of the two weights. We made use of these weights in all distributions presented in the remainder of this section.

Figure 3 shows the distributions of unobscured (blue shaded histograms) and obscured AGN (red dashed line histograms). The top panel presents the SFR distributions of the two AGN classes. The (weighted) median log SFR of the unobscured and obscured AGN is 0.82 and 0.57, respectively (Table 2). Applying a Kolmogorov-Smirnov (KS) test yielded a p -value

of 0.10 (also shown in the legend of the plot). Similar p -value were obtained by applying a Mann-Whitney test (MW; p -value = 0.14) and a Kuiper (p -value = 0.32) test. Therefore, the difference of 0.25 dex does not appear statistically significant (two distributions differ with a statistical significance of $\sim 2\sigma$ for a p -value of 0.05).

The bottom panel of Fig. 3 shows the M_* distributions of obscured (blue shaded histogram) and unobscured (red dashed line) AGN. The weighted median of the log M_* is 10.86 and 10.95 for unobscured and obscured AGN, respectively. Although the difference is small, it appears to be statistically significant (Table 2). Specifically, the p -value derived from the KS test was 0.02. Similar p -value were also obtained by applying MW and Kuiper tests (< 0.05). We note that the (weighted) standard deviations (SDs) of the two populations are 11.22 (obscured) and 11.13 (unobscured). The (weighted) 95% confidence intervals (CI) are 10.91–11.30 and 10.99–11.07 for the obscured and unobscured AGN, respectively. Therefore, based on our results, obscured AGN tend to live in more massive systems, and their hosts have a lower SFR compared to their unobscured counterparts. However, only the M_* difference appears to be statistically significant.

Furthermore, we explored whether our outcomes are influenced by potential redshift evolution within the $z < 0.7$ redshift range encompassed by our dataset. For that purpose, we split the AGN sample into two redshift bins using the median value of the $z < 0.7$ dataset (i.e. at $z = 0.21$). The results do not appear redshift dependent since similar trends and p -values were obtained. Additionally, we examined whether our findings might be sensitive to uncertainties associated with photometric redshift estimates. To address this concern, we narrowed down our analysis to include only sources with spectroscopic redshifts. We obtained similar results in this restricted subset.

Most previous studies that examined the host galaxy properties of X-ray obscured and unobscured AGN did not find (significant) differences for the SFR and M_* of the hosts of the two AGN populations. Specifically, Masoura et al. (2021) and Mountrichas et al. (2021c) studied the SFR and M_* of X-ray obscured and unobscured AGN at $0 < z < 3.5$ using data from the XMM-XXL and the Boötes fields, respectively, and concluded that both AGN classes live in galaxies with similar properties (see also Merloni et al. 2014). We note that the aforementioned studies did not account for the uncertainties in the N_H values and applied a lower N_H threshold ($N_H = 10^{21.5} \text{ cm}^{-2}$) to classify their AGN. However, Lanzuisi et al. (2017) studied AGN at $0.1 < z < 4$ in the COSMOS field and found that the average N_H shows a clear positive correlation with M_* but not with the SFR. Studies that used optical criteria (e.g. optical spectra) to classify the AGN into type 1 and type 2 found that the two AGN types live in galaxies with similar SFR, but type 2 sources tend to reside in more massive systems, by ~ 0.3 dex, both at low redshift ($z < 1$; Mountrichas et al. 2021c) and at high redshift ($z < 3.5$; Zou et al. 2019).

More recently, Georgantopoulos et al. (2023) compared the stellar populations and M_* , among others, of X-ray obscured and unobscured AGN host galaxies in the COSMOS field at $z \sim 1$ using $N_H = 10^{23} \text{ cm}^{-2}$ to classify their sources. Their analysis showed that the distribution of M_* of obscured AGN is skewed to a higher M_* compared to unobscured AGN. Specifically, they found that heavily obscured AGN live in galaxies that have a higher M_* by 0.13 dex compared to unobscured sources. Although the difference was small, it was statistically significant (p -value = 1.3×10^{-3}). Notably, their results are in excellent agreement with our findings. They also found that heavily

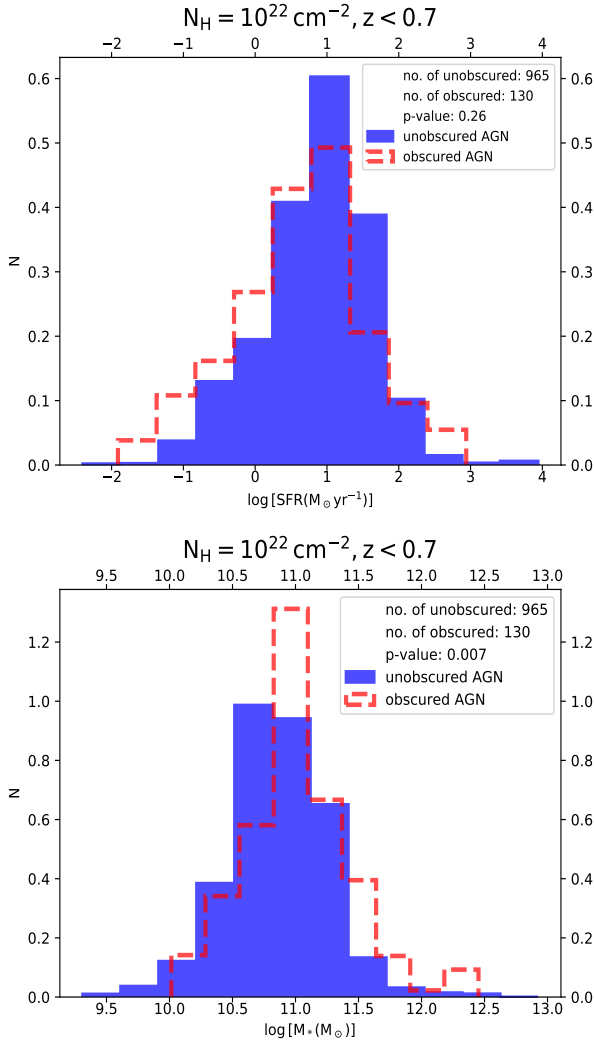


Fig. 4. Similar to Fig. 3 but using a limit of $N_{\text{H}} = 10^{22} \text{ cm}^{-2}$ to classify AGN (taking into account the errors of the N_{H} measurements).

obscured AGN tend to live in systems with older stars compared to unobscured AGN. This is consistent with our finding of a lower SFR for heavily obscured AGN hosts compared to those that are unobscured, although in our measurements the difference did not appear statistically significant.

Georgantopoulos et al. (2023) suggested that a possible cause for the discrepant results among previous studies could be the different N_{H} thresholds that were used. Indeed, when they lowered the N_{H} value used to classify their AGN, the statistical significance of the differences detected in the host galaxy properties of the two AGN classes was lower (see their Fig. 13). To verify this hypothesis, we lowered the N_{H} threshold utilised for our AGN classification to $N_{\text{H}} = 10^{22} \text{ cm}^{-2}$ using the lower and upper limits of N_{H} specified at the outset of this section and repeated the analysis. The findings are showcased in Fig. 4 and Table 2. Results similar to those presented in Fig. 3 emerged. Specifically, obscured AGN tend to inhabit more massive systems (by 0.12 dex) and have a lower SFR (by 0.26 dex) compared to unobscured AGN. However, among these differences, only the variation in M_* demonstrates statistical significance. It is observed that the (weighted) standard deviation of the two populations is 11.54 for the obscured AGN and 11.29 for the unobscured AGN. The (weighted) 95% confidence intervals are

11.10–11.40 for the obscured AGN and 11.00–11.10 for the unobscured AGN. Nonetheless, if we ignore the errors of the N_{H} measurements, effectively classifying AGN based solely on their N_{H} values without considering the limits of the measurements and implement a threshold at $N_{\text{H}} = 10^{22} \text{ cm}^{-2}$, similar to what most prior studies have used for AGN classification, we uncover a marginally statistically significant difference in the M_* distributions of the two AGN types (p -value = 0.052) and no statistically significant difference in terms of the SFR distributions of the obscured and unobscured AGN.

An alternative hypothesis proposed by Georgantopoulos et al. (2023) is that the variations in results across different studies could be attributed to the diverse luminosity ranges covered by the respective samples. For instance, AGN in the Boötes and XMM-XXL fields (Masoura et al. 2021; Mountrichas et al. 2021c) probe higher luminosities compared to those probed by sources in the COSMOS field (Lanzuisi et al. 2017; Georgantopoulos et al. 2023). This is also true when we compare the results between studies that used X-ray and optical criteria to classify the AGN. The latter have either used sources in the COSMOS field (e.g. Zou et al. 2019) that mainly probe low to intermediate L_{X} AGN, or they have restricted their analysis to low luminosity systems at low redshift (e.g. Mountrichas et al. 2021c). To examine this hypothesis, we restricted our X-ray dataset to luminous sources by applying a luminosity cut at $\log[L_{\text{X}}(\text{erg s}^{-1}) > 44]$ (at $z < 0.7$), and we classified the AGN using an N_{H} value of 10^{22} (using the lower and upper limits of N_{H}) and repeated the analysis. There are 17 luminous and obscured AGN and 223 luminous and unobscured AGN. We detected a difference of 0.35 dex (based on the weighted median values) in the SFR of the two AGN populations. The obscured AGN appear to live in more massive systems compared to unobscured AGN (by 0.06 dex). However, none of these differences appeared to be statistically significant (p -value = 0.52 and 0.17 for the SFR and M_* , respectively).

5.2. Eddington ratio of X-ray obscured and unobscured active galactic nuclei

The difference with the highest statistical significance that Georgantopoulos et al. (2023) reported was between the n_{Edd} of obscured and unobscured sources (see e.g. their Table 3). Prompted by their results, we examined this difference in our dataset. For the dataset used in this part of our analysis, we did not have any available M_{BH} , and therefore there were no n_{Edd} measurements for our sources. Cross-matching our sample with the Wu & Shen (2022) catalogue (see Sect. 2) in which there are available n_{Edd} measurements would constrain our dataset to only broad-line sources and exclude narrow-line AGN. In the next section, we examine whether n_{Edd} depends on N_{H} (for broad-line AGN). In order to include both broad- and narrow-line sources in our investigation, in place of n_{Edd} , we examined the specific black hole accretion rate, λ_{SBHAR} , of obscured and unobscured AGN. We note that λ_{SBHAR} is the rate of the accretion onto the SMBH relative to the M_* of the host galaxy. It is often used as a proxy of n_{Edd} , particularly when M_{BH} measurements are not available (e.g. Georgakakis et al. 2017; Aird et al. 2018; Mountrichas et al. 2021c; Pouliasis et al. 2022). For the calculation of λ_{SBHAR} , the following expression was used (e.g. Aird et al. 2018):

$$\lambda_{\text{SBHAR}} = \frac{k_{\text{bol}} L_{\text{X}, 2-10 \text{ keV}}}{1.26 \times 10^{38} \text{ erg s}^{-1} \times 0.002 \frac{M_*}{M_{\odot}}}, \quad (1)$$

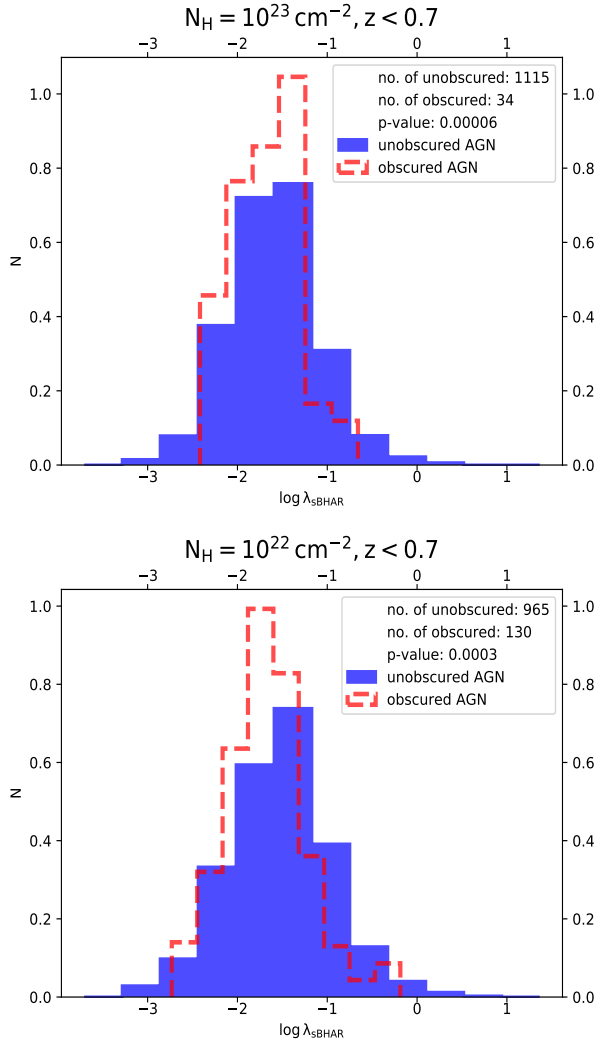


Fig. 5. Distributions of λ_{sBHAR} for obscured and unobscured AGN. The top panel presents the distributions using an N_{H} threshold of 10^{23} cm^{-2} for the source classification. The bottom panel presents the results using $N_{\text{H}} = 10^{22} \text{ cm}^{-2}$ to characterise sources. In both cases, the errors of the N_{H} measurements have been taken into account (see text for more details). Distributions are also weighted based on the redshift and L_{X} of the sources.

where k_{bol} is a bolometric correction factor that converts the X-ray luminosity to AGN bolometric luminosity. We adopted the value of $k_{\text{bol}} = 25$ (e.g. Georgakakis et al. 2017; Aird et al. 2018; Mountrichas et al. 2021c, 2022c).

Figure 5 presents the λ_{sBHAR} distributions of obscured and unobscured AGN using different N_{H} thresholds to classify sources, as indicated at the top of each panel (taking into account the errors on the N_{H} measurements). All distributions are weighted based on the L_{X} and redshift of the sources. Table 2 presents the (weighted) median $\log \lambda_{\text{sBHAR}}$ of the obscured and unobscured AGN for $N_{\text{H}} = 10^{23} \text{ cm}^{-2}$ and $N_{\text{H}} = 10^{22} \text{ cm}^{-2}$. We found a difference of ~ 0.1 – 0.2 dex in the λ_{sBHAR} values of the two populations. Specifically, we found obscured sources tend to have, on average, a lower λ_{sBHAR} compared to unobscured sources. Based on the p -values derived using a KS test, this difference has a high statistical significance, regardless of the N_{H} limit used. Similar p -values were found by applying MW and Kuiper tests.

Our results are in agreement with those reported in Georgantopoulos et al. (2023). We note that the difference we found appears smaller compared to the difference presented in the aforementioned study (~ 0.3 dex). As we have already pointed out, we used stricter criteria in our analysis for the classification of AGN as obscured and unobscured compared to what was used in Georgantopoulos et al. (2023). Moreover, in Georgantopoulos et al. (2023), for the calculation of n_{Edd} , they applied the same bolometric correction on L_{X} to infer L_{bol} as in this study. However, they used M_{BH} measurements derived by stellar velocity dispersions, σ ; that is, they utilised a different scaling relation compared to our work.

We concluded that the obscured AGN tend to live in more massive systems compared to unobscured AGN at $z < 0.7$. The difference in M_* is small (~ 0.1 dex), but it appears to be statistically significant. Obscured sources also live in hosts that have a lower SFR, by ~ 0.25 dex, than unobscured AGN; however, this difference is not statistically significant ($< 2\sigma$). Moreover, neither of these differences appears to be statistically significant for luminous AGN ($\log [L_{\text{X}}(\text{erg s}^{-1}) > 44]$) and/or when less strict criteria are used for the source classification (i.e. errors on N_{H} are ignored). Based on our analysis, the difference between the two AGN populations with the highest statistical significance is that regarding the λ_{sBHAR} , which is a proxy of the n_{Edd} .

5.3. Comparative analysis of super massive black hole characteristics, X-ray spectral attributes, and host galaxy properties

In the second part of our analysis, we examined the relationships among L_{bol} , M_{BH} , and M_* as a function of the X-ray obscuration (N_{H}). We also investigated the correlation between the powerlaw slope, Γ , of the spectral model with the n_{Edd} . For that purpose, we used the 271 X-ray AGN that are in common between the XMM catalogue and the Wu & Shen (2022) catalogue (see Sect. 4). Here and in the following (sub-) sections, we characterise as AGN with high N_{H} those sources with $\log N_{\text{H}} \geq 22$ using the mode value of N_{H} that is available in our catalogue (i.e. without using the lower and upper limits of N_{H}). There are 23 AGN with high N_{H} values and 248 AGN with low N_{H} values in our dataset. The reason for using this threshold is that it facilitates a better comparison with previous studies. Furthermore, we note that characterising an AGN with high N_{H} based on requiring the lower limit of N_{H} to be higher than 10^{23} cm^{-2} (10^{22} cm^{-2}) would result in zero (seven) sources.

Figures 6–8 present the distributions of L_{X} , M_* , and M_{BH} as a function of redshift, respectively, for the 271 X-ray AGN. All three properties increase with redshift regardless of the N_{H} value of the source. A Spearman correlation analysis revealed that there is a significant correlation between L_{X} , M_* , and M_{BH} with redshift, albeit these correlations appear higher in the case of sources with $N_{\text{H}} < 10^{22} \text{ cm}^{-2}$ (Table 3). We note that in this part of our analysis, only broad-line (type 1) sources were included (see Sect. 2).

5.3.1. Bolometric luminosity versus black hole mass

In Fig. 9, we plot the L_{bol} as a function of M_{BH} . We chose to plot the L_{bol} measurements that are available in the Wu & Shen (2022) catalogue. We note that their L_{bol} calculations are in excellent agreement with the L_{bol} measurements from CIGALE. Specifically, the mean difference of the two calculations is 0.04 dex (with a dispersion of 0.36), and thus this choice does not affect our results and conclusions. The lines correspond to

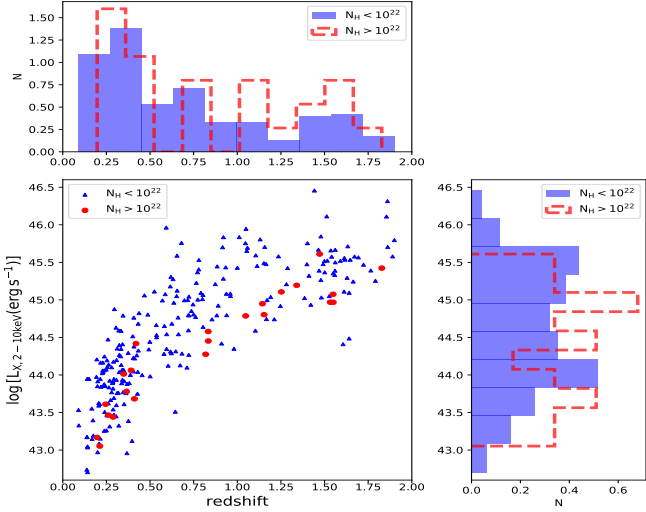


Fig. 6. X-ray luminosity, L_X , as a function of redshift. AGN with $\log N_H > 10^{22} \text{ cm}^{-2}$ are marked with red circles, whereas sources with $\log N_H < 10^{22} \text{ cm}^{-2}$ are marked with blue triangles.

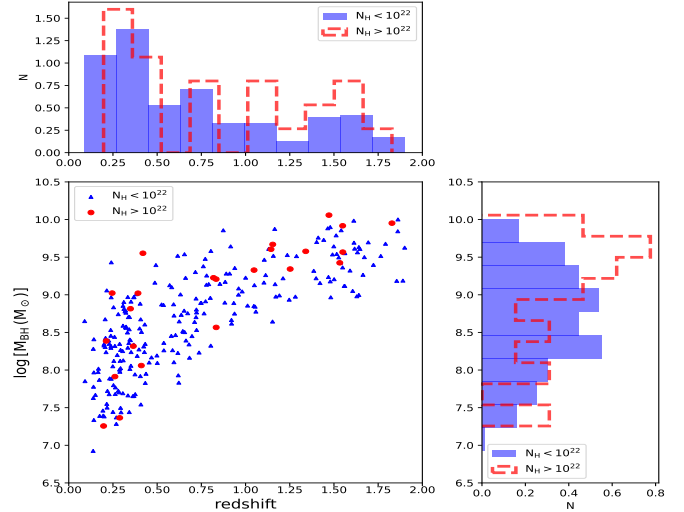


Fig. 8. Black hole mass, M_{BH} , as a function of redshift. AGN with $\log N_H > 10^{22} \text{ cm}^{-2}$ are marked with red circles, whereas sources with $N_H < 10^{22} \text{ cm}^{-2}$ are marked with blue triangles.

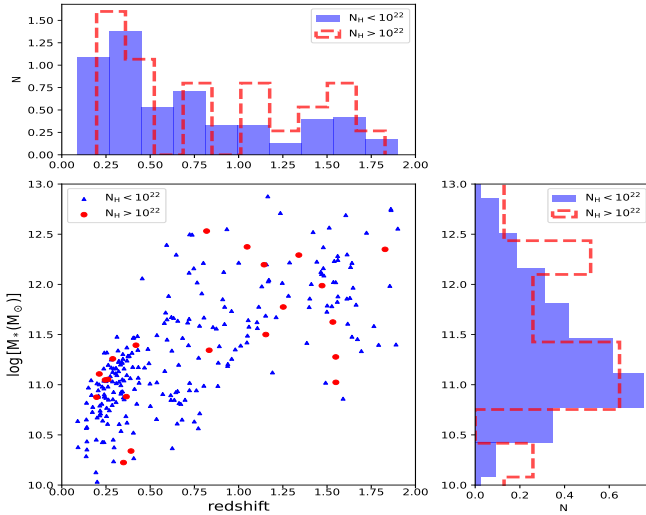


Fig. 7. Stellar mass, M_* , as a function of redshift. AGN with $\log N_H > 10^{22} \text{ cm}^{-2}$ are marked with red circles, whereas sources with $N_H < 10^{22} \text{ cm}^{-2}$ are marked with blue triangles.

$L_{bol} = L_{Edd}$ (black long-dashed line), $L_{bol} = 0.1 L_{Edd}$ (green solid line), and $L_{bol} = 0.01 L_{Edd}$ (red dotted line). The vast majority of our AGN lie between Eddington ratios of 0.01 and 1, with a median value of $n_{Edd} = 0.14$, in agreement with previous studies (e.g. Trump et al. 2009; Lusso et al. 2012; Sun et al. 2015; Suh et al. 2020; Mountrichas 2023). Different symbols correspond to different redshift intervals, as indicated in the legend of the plot. The median value of n_{Edd} is 0.09 and 0.24 at $z < 0.7$ and $0.7 < z < 1.9$, respectively.

The measurements in Fig. 9 are colour-coded based on the N_H of the sources. Although the AGN sample used in this part of our analysis consists of type 1 sources, there are a few AGN that present low levels of X-ray obscuration ($N_H \sim 10^{22} \text{ cm}^{-2}$). It is known that X-ray and optical obscuration do not necessarily coincide and several instances have been documented in the literature where type 1 AGN exhibit X-ray obscuration (e.g. Mateos et al. 2005, 2010; Scott et al. 2011; Shimizu et al. 2018; Kamraj et al. 2019; Masoura et al. 2020). Regarding the n_{Edd}

Table 3. p -values obtained from Spearman correlation analysis, assessing the correlations among L_X , M_* , M_{BH} , and redshift.

	$N_H < 10^{22} \text{ cm}^{-2}$	$N_H > 10^{22} \text{ cm}^{-2}$
	p -value	p -value
$\log L_X$ -redshift	5×10^{-72}	3×10^{-12}
$\log M_*$ -redshift	2×10^{-43}	6×10^{-4}
$\log M_{BH}$ -redshift	7×10^{-53}	2×10^{-7}

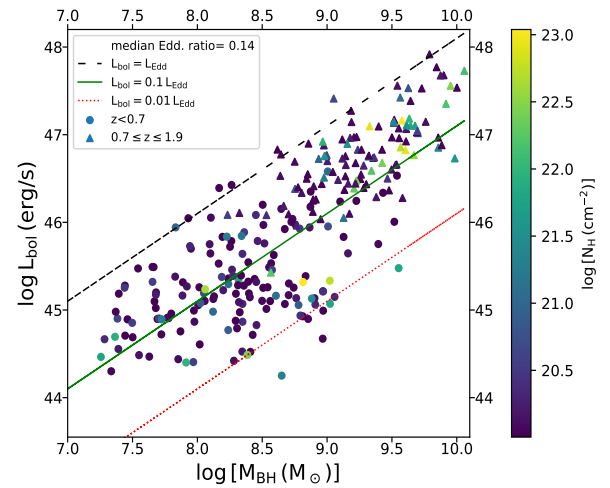


Fig. 9. Bolometric luminosity, L_{bol} , as a function of M_{BH} . Different symbols correspond to different redshift intervals, as indicated in the legend. The lines correspond to $L_{bol} = L_{Edd}$ (black dashed line), $L_{bol} = 0.1 L_{Edd}$ (green solid line) and $L_{bol} = 0.01 L_{Edd}$ (red dotted line). Measurements are colour-coded based on the N_H of each source.

values of X-ray sources with high and low N_H values, we did not find a difference among the two AGN populations. Specifically, the median values are $n_{Edd} = 0.12$ and 0.15 for AGN with $N_H > 10^{22} \text{ cm}^{-2}$ and AGN with $N_H < 10^{22} \text{ cm}^{-2}$, respectively. A KS test yielded a p -value of 0.83 for the n_{Edd} distributions of the two AGN classes.

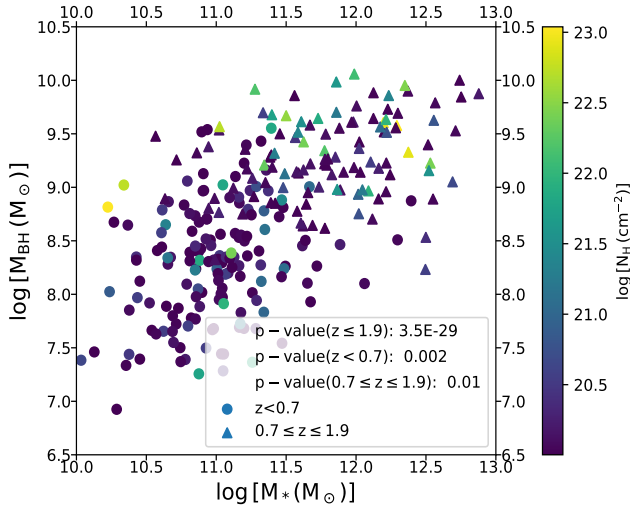


Fig. 10. Black hole mass, M_{BH} , as a function of M_* . Different symbols correspond to different redshift bins, as indicated in the legend. The p -values obtained by applying a Spearman correlation analysis for the full redshift range ($z < 1.9$) as well as at low redshift ($z < 0.7$) and high redshift ($0.7 < z < 1.9$) are also shown. Measurements are colour-coded based on the N_{H} of each source.

5.3.2. Black hole mass versus stellar mass

Next in our analysis, we examined the correlation between M_{BH} and M_* . The results are presented in Fig. 10. A strong correlation was detected between the two parameters. Applying a Spearman correlation analysis yielded a p -value of 3.5×10^{-29} . A similar value was found using a Kendall correlation analysis (p -value = 8.1×10^{-26}). Strong correlations between M_{BH} and M_* were also found when we split the dataset into two redshift intervals. The p -values are shown in the legend of Fig. 10. In this case the correlations, although strong, were weaker compared to the correlation found for our full sample. This can be attributed to the narrower range of M_{BH} and M_* probed by the sources within distinct redshift intervals compared to the sources encompassing the entire redshift range (see Figs. 7 and 8). To validate this conjecture, we employed the AGN dataset spanning the complete redshift range ($z \leq 1.9$); we restricted the (log of) M_* and M_{BH} ranges within 11.0–13.0 and 8.5–10, respectively (resembling the intervals embraced by AGN residing within $0.7 \leq z \leq 1.9$); and we carried out a Spearman correlation analysis. This procedure resulted in a p -value of 0.008. Similarly, we obtained a p -value of 6×10^{-4} by limiting the M_* and M_{BH} ranges to 10.0–11.5 and 7.0–9.5 (akin to the intervals pertinent to AGN existing within $z < 0.7$).

Prompted by the results of Sarria et al. (2010), who examined three X-ray AGN at $z = 1$ –2, with $N_{\text{H}} = 10^{22.5-23.0} \text{ cm}^{-2}$ and observed that they were consistent with the local $M_{\text{BH}} - M_*$ relation, we colour coded the symbols in Fig. 10 based on the N_{H} values of the sources. We noticed that sources with increased N_{H} have a higher M_{BH} for similar M_* compared to sources with a lower N_{H} . This is better illustrated in Fig. 11, where we mark AGN with N_{H} values above and below 10^{22} cm^{-2} differently, as indicated in the legend of the plot. The different lines in Fig. 11 indicate the best fits for the various subsets acquired through the application of a least-squares analysis. As mentioned above, AGN with higher N_{H} values tend to have more massive black holes compared to AGN with lower N_{H} values at similar M_* , at least up to $\log [M_*(M_{\odot})] = 12$.

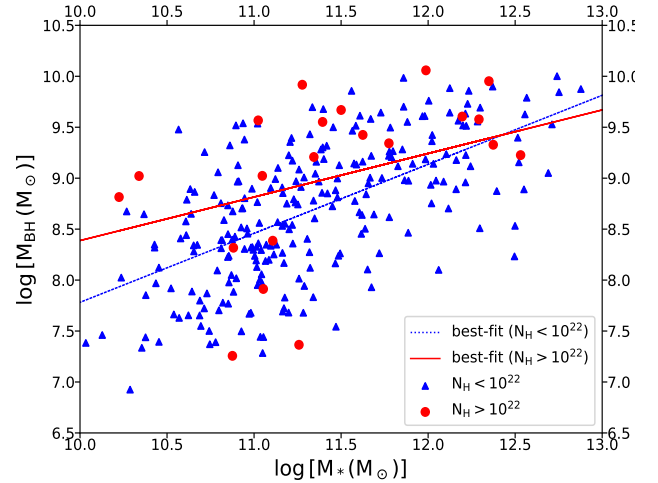


Fig. 11. Black hole mass, M_{BH} , as a function of M_* for sources with $\log N_{\text{H}} > 10^{22} \text{ cm}^{-2}$ (red circles) and sources with $\log N_{\text{H}} < 10^{22} \text{ cm}^{-2}$ (blue triangles). Different lines represent the best fits of the different subsets, as indicated in the legend.

We also examined the ratio of M_{BH}/M_* as a function of redshift. Based on the results presented in the top panel of Fig. 12, the M_{BH}/M_* does not evolve with cosmic time up to $z < 2$. The median $\log(M_{\text{BH}}/M_*)$ value was found at -2.63 . This value is in agreement with most previous studies that measured the M_{BH}/M_* ratio in the local Universe (e.g. -2.85 ; Häring & Rix 2004) as well as at high redshifts (e.g. Suh et al. 2020; Mountrichas 2023). The bottom panel of Fig. 12 presents the distributions of the M_{BH}/M_* ratio at different redshift intervals. The median value of the M_{BH}/M_* ratio at $z < 0.7$ is -2.69 , and at $0.7 < z < 1.9$, it is -2.55 . The application of KS tests confirmed that the distributions are similar (p -values > 0.9 among all redshift intervals).

The results that appear in the top panel of Fig. 12 are colour-coded based on the N_{H} of the sources. Sources with higher N_{H} values seem to have a higher M_{BH}/M_* ratio. To examine this further, in Fig. 13, we plot the M_{BH}/M_* ratio as a function of N_{H} . The blue line shows the best fit of the $\frac{M_{\text{BH}}}{M_*} - \log N_{\text{H}}$ relation for $\log N_{\text{H}} < 22 \text{ cm}^{-2}$, whereas the red line shows the best fit for $\log N_{\text{H}} > 22 \text{ cm}^{-2}$. The blue line is nearly flat, with a slope of 0.014 (standard error 0.079), which indicates that the M_{BH}/M_* ratio is almost constant for AGN with $\log N_{\text{H}} < 22 \text{ cm}^{-2}$. However, the best fit for AGN with $\log N_{\text{H}} > 22 \text{ cm}^{-2}$ has a slope of 0.69 (standard error 0.24), which indicates that the M_{BH}/M_* ratio increases with N_{H} for X-ray AGN with high N_{H} values. A Spearman correlation analysis revealed a p -value = 0.06 for the correlation between $\frac{M_{\text{BH}}}{M_*} - \log N_{\text{H}}$ for sources with $\log N_{\text{H}} > 22 \text{ cm}^{-2}$, which indicates a statistical significance of $\sim 2\sigma$. The median value of the $\log M_{\text{BH}}/M_*$ ratio is -2.40 and -2.66 for AGN with $N_{\text{H}} > 10^{22} \text{ cm}^{-2}$ and $N_{\text{H}} < 10^{22} \text{ cm}^{-2}$, respectively. We note, though, that a larger number of sources with $N_{\text{H}} > 10^{22} \text{ cm}^{-2}$ is required to formulate robust conclusions.

In the preceding sections, we observed that obscured AGN live, on average, in galaxies with a higher M_* compared to unobscured AGN. Moreover, obscured AGN tend to have a higher M_{BH} compared to their unobscured counterparts at similar M_* . When combined with the higher M_{BH}/M_* ratio within the AGN population displaying elevated N_{H} values, assuming this holds true, it implies that the SMBH growth in the obscured phase is higher than the galaxy growth. This may suggest that the growth

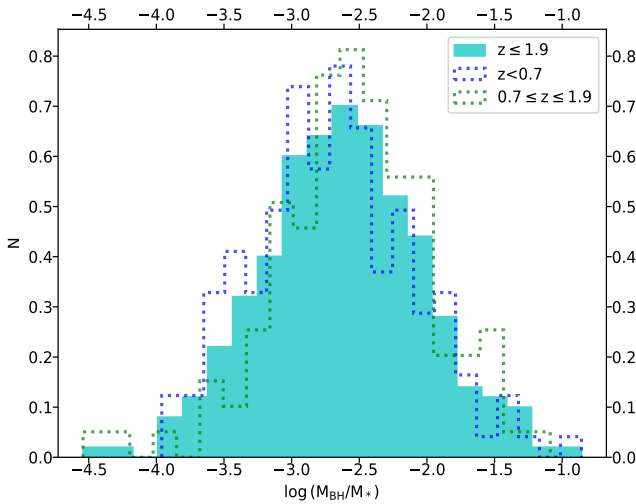
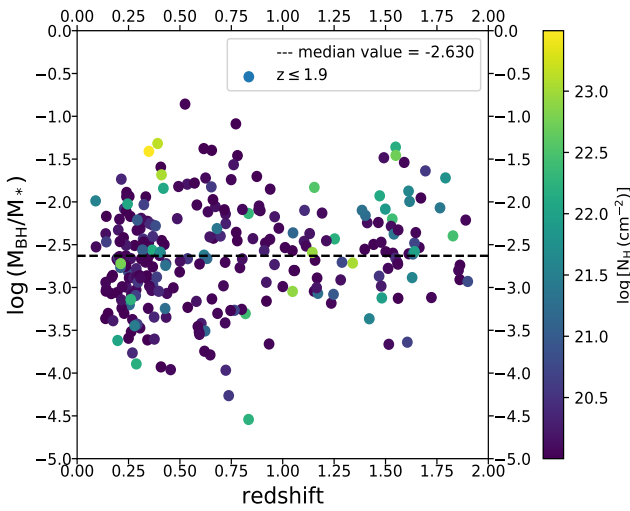


Fig. 12. Ratio of M_{BH} to M_* . The top panel presents the $M_{\text{BH}} - M_*$ ratio as a function of redshift, and the bottom panel shows the distributions of the $M_{\text{BH}} - M_*$ ratio at different redshift intervals.

of the M_{BH} occurs first, while the early stellar mass assembly may not be so efficient (Mountrichas et al. 2023).

5.3.3. Powerlaw slope versus Eddington ratio

We also investigated if there is a correlation between the powerlaw slope, Γ , of the X-ray spectral model and the n_{Edd} . The results are shown in the top panel of Fig. 14. A strong correlation was found between Γ and n_{Edd} (p -value = 8.1×10^{-7} , applying both a Spearman and a Kendall correlation analysis). However, the correlation between the two parameters was also strong when we split the dataset into two redshift intervals; at $0.7 < z < 1.9$, the p -value appears higher compared to the p -value obtained at $z < 0.7$ (see legend in the top panel of Fig. 14). This is most probably due to the different lines used for the calculation of the M_{BH} and not a result of cosmic evolution. Risaliti et al. (2009) reported a strong correlation between the two parameters when the M_{BH} was calculated using the $\text{H}\beta$ line, while the authors reported a weaker correlation when the M_{BH} was measured using the Mg II line. There are only 12 sources in our dataset with $0.7 < z < 1.9$ that have M_{BH} calculations from both lines; there-

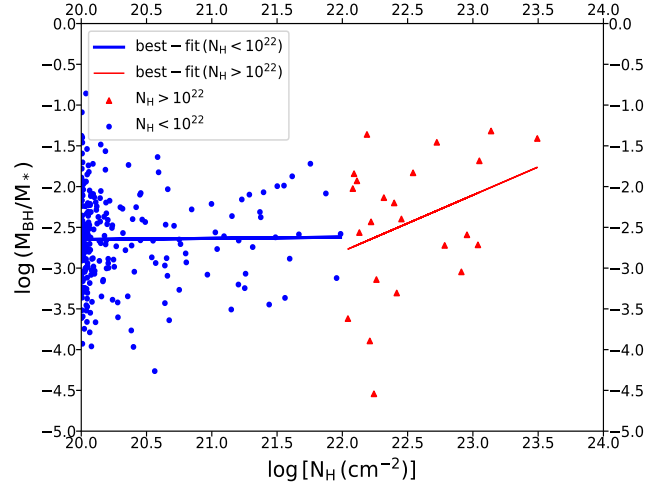


Fig. 13. Ratio of M_{BH} to M_* as a function of N_{H} .

fore, we could not test, in a robust manner, this hypothesis further. We also split the dataset into high and low L_X , by applying a cut at $\log[L_X(\text{ergs}^{-1})] = 44$. A strong correlation was found both at high and low L_X . The application of the Spearman correlation analysis gave p -values = 5.3×10^{-4} and 3.1×10^{-9} for $\log[L_X(\text{ergs}^{-1})] > 44$ and $\log[L_X(\text{ergs}^{-1})] < 44$, respectively.

We further examined if this correlation between Γ and n_{Edd} holds for different N_{H} values. The results are shown in the bottom panel of Fig. 14. A strong correlation was found between Γ and n_{Edd} for AGN with $N_{\text{H}} < 10^{22} \text{ cm}^{-2}$. Application of the Spearman correlation analysis yielded p -value = 1.35×10^{-6} (p -value = 1.44×10^{-6} , applying Kendall's correlation analysis). No correlation was found, though, for the AGN population with $N_{\text{H}} > 10^{22} \text{ cm}^{-2}$ (p -value = 0.47 and 0.53, from Spearman and Kendall correlation analysis, respectively). The different lines shown in the figure represent the best fits of the $\Gamma - n_{\text{Edd}}$ relation for the total AGN sample (black dashed line; $\Gamma = 0.315 \times n_{\text{Edd}} + 0.294$), the AGN with $N_{\text{H}} < 10^{22} \text{ cm}^{-2}$ (blue line; $\Gamma = 0.306 \times n_{\text{Edd}} + 2.303$), and for AGN with $N_{\text{H}} > 10^{22} \text{ cm}^{-2}$ (red line; $\Gamma = 0.083 \times n_{\text{Edd}} + 1.565$). Similar results were obtained when we split the two AGN populations into two redshift intervals at $z = 0.7$. Furthermore, our observations hold when considering the associated uncertainties of Γ and n_{Edd} . This was verified, by utilising the linmix module (Kelly 2007), which performs a linear regression between two parameters by repeatedly perturbing the datapoints within their uncertainties.

We find it worth pointing out that in Fig. 14 there are some sources with non-physical values ($\Gamma > 2.5$ or $\Gamma < 1.5$). Although their occurrence is relatively low among AGN with $N_{\text{H}} < 10^{22} \text{ cm}^{-2}$ (15%), it becomes more pronounced (57%) for AGN with higher N_{H} values. To examine whether this might influence the absence of a correlation between Γ and n_{Edd} for AGN with $N_{\text{H}} > 10^{22} \text{ cm}^{-2}$, we opted to exclude these sources and repeated the correlation analysis. However, even after this exclusion, we still did not observe a significant correlation between the two parameters for sources with elevated N_{H} values. We find it essential to note, however, that this refinement in the analysis left us with a considerably reduced sample size, comprising only ten AGN with $N_{\text{H}} > 10^{22} \text{ cm}^{-2}$.

The X-ray spectral index is sensitive to the properties of the accretion disc, such as temperature and ionisation state. Therefore, a correlation between the X-ray spectral index and n_{Edd} for AGN with $N_{\text{H}} < 10^{22} \text{ cm}^{-2}$ may imply that changes in the

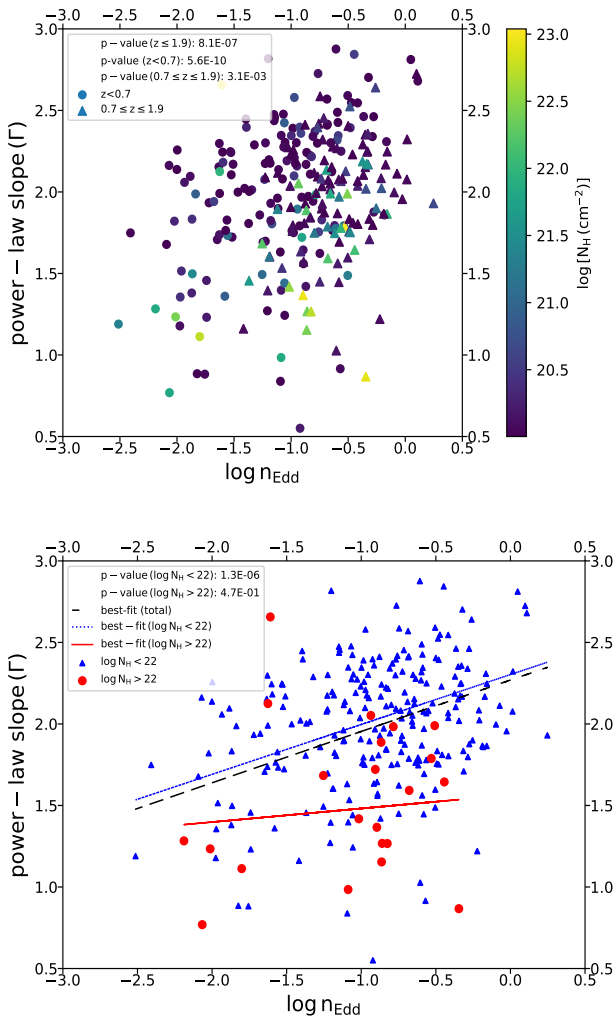


Fig. 14. Spectral photon index, Γ , as a function of n_{Edd} . In the top panel, different symbols correspond to different redshift intervals, as indicated in the legend. The results are colour-coded based on the N_{H} values of the sources. The p -values obtained by applying a Spearman correlation analysis are shown in the legend. The bottom panel shows the same relation but for X-ray AGN with $N_{\text{H}} > 10^{22} \text{ cm}^{-2}$ (red circles) and AGN with $N_{\text{H}} < 10^{22} \text{ cm}^{-2}$ (blue triangles). The p -values for the $\Gamma - n_{\text{Edd}}$ correlation for each AGN population are presented in the legend of the plot. The different lines correspond to the best fits using the total AGN sample (black dashed line), AGN with $N_{\text{H}} > 10^{22} \text{ cm}^{-2}$ (red solid line), and AGN with $N_{\text{H}} < 10^{22} \text{ cm}^{-2}$ (blue line).

accretion rate can alter the structure and properties of the accretion disc, influencing the X-ray emission. The X-ray emission is also associated with a hot, optically thin corona of electrons above the accretion disc. The properties of the corona, such as its temperature and optical depth, can impact the X-ray spectral index. Thus, changes in the n_{Edd} may lead to variations in the corona properties, affecting the X-ray spectrum. The AGN with $N_{\text{H}} < 10^{22} \text{ cm}^{-2}$ allow for a clearer view of the inner regions of the accretion disc and the corona. Furthermore, in AGN with low N_{H} , a more direct view of the accretion disc may allow for a better determination of the Eddington ratio.

Additionally, we investigated if this lack of correlation between the two parameters for the AGN population with $N_{\text{H}} > 10^{22} \text{ cm}^{-2}$ is due to the small number of available sources. For that purpose, we randomly selected an equal number of AGN with $N_{\text{H}} < 10^{22} \text{ cm}^{-2}$ to that with $N_{\text{H}} > 10^{22} \text{ cm}^{-2}$, and we

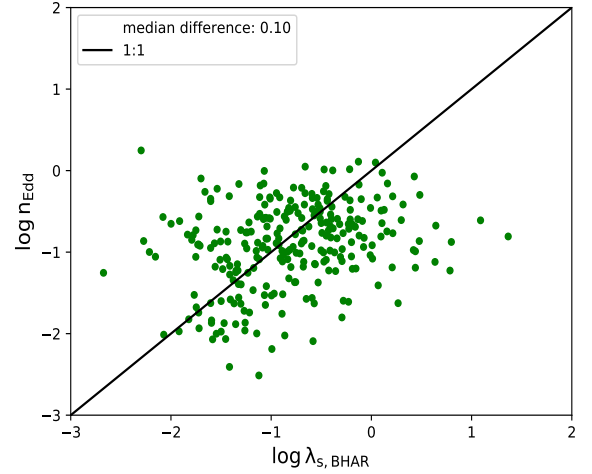


Fig. 15. Eddington ratio, n_{Edd} , vs. $\lambda_{\text{s,BHAR}}$ for the 271 AGN that are common between the XMM sample and the Wu & Shen (2022) catalogue.

measured the correlation between Γ and n_{Edd} . After 500 repetitions of this process, we obtained a median p -value of 0.047 from Spearman analysis (Kendall's correlation analysis yielded p -value = 0.091). The p -value obtained for the simulated AGN with $N_{\text{H}} < 10^{22} \text{ cm}^{-2}$ is about an order of magnitude lower compared to that obtained from the AGN with $N_{\text{H}} > 10^{22} \text{ cm}^{-2}$. This indicates that the lack of correlation between Γ and n_{Edd} for AGN with $N_{\text{H}} > 10^{22} \text{ cm}^{-2}$ is intrinsic and not due to their smaller sample size. This result aligns with the Comptonisation models, wherein variations in the accretion rate have a more pronounced impact on the soft spectral component (which gets lost in absorbed sources) compared to the hard powerlaw photon index.

As already noted, $\lambda_{\text{s,BHAR}}$ is often used as a proxy of n_{Edd} . Lopez et al. (2023) used X-ray selected AGN in the miniJ-PAS footprint and found, among other things, that the n_{Edd} and $\lambda_{\text{s,BHAR}}$ have a difference of 0.6 dex. They attributed this difference to the scatter on the $M_{\text{BH}} - M_*$ relation of their sources. A difference between n_{Edd} and $\lambda_{\text{s,BHAR}}$ was also reported by Mountrichas & Buat (2023), albeit lower (~ 0.25 dex), using AGN in the XMM-XXL field. Figure 15 presents a comparison between the two parameters for the 271 X-ray AGN that are in common between the XMM catalogue and the Wu & Shen (2022) catalogue. We found that, overall, there is good agreement between n_{Edd} and $\lambda_{\text{s,BHAR}}$, with a median difference of 0.10 dex. We stress that this comparison includes only broad-line AGN. We also confirm that this difference does not depend on N_{H} , at least up to $N_{\text{H}} = 10^{22.5-23} \text{ cm}^{-2}$, as probed by our dataset.

Since the n_{Edd} measurements are in agreement with the $\lambda_{\text{s,BHAR}}$ calculations, we then examined the correlation between Γ and $\lambda_{\text{s,BHAR}}$. We found similar results as those between Γ and n_{Edd} . Specifically, a strong correlation was found between the two parameters for AGN with $N_{\text{H}} < 10^{22} \text{ cm}^{-2}$ (p -value = 2.8×10^{-3}), but no correlation was detected for sources with $N_{\text{H}} > 10^{22} \text{ cm}^{-2}$ (p -value = 0.95). Prompted by these results, we utilised the larger AGN dataset used in Sect. 5.1 (i.e. before matching the XMM sources with the Wu & Shen 2022, catalogue) to examine the correlation between Γ and $\lambda_{\text{s,BHAR}}$ for the two AGN populations. This allowed us to investigate the $\Gamma - \lambda_{\text{s,BHAR}}$ relation using a significantly larger sample of obscured sources (130 AGN) that has been defined with stricter

criteria (i.e. taking into account the uncertainties associated with N_{H}) and, more importantly, to include narrow-line (type 2) AGN in our investigation. A Spearman correlation analysis yielded a p -value of 1.8×10^{-11} for AGN with $N_{\text{H}} < 10^{22} \text{ cm}^{-2}$ and 0.31 for AGN with $N_{\text{H}} > 10^{22} \text{ cm}^{-2}$. We conclude that Γ and n_{Edd} are correlated at all redshift and L_{X} probed by our dataset. However, we did not detect such a correlation for AGN with increased N_{H} values ($N_{\text{H}} > 10^{22} \text{ cm}^{-2}$).

Previous studies have found contradictory results regarding whether there is a correlation between Γ and n_{Edd} . Shemmer et al. (2008) used 35 unabsorbed type 1 radio quiet (RQ) AGN at $z < 3.2$ (25 out of the 35 sources were at $z < 0.5$) and found a significant correlation between Γ and n_{Edd} . They concluded that a measurement of Γ and L_{X} can provide an estimate of n_{Edd} and M_{BH} with a mean uncertainty of a factor less than or equal to three. Brightman et al. (2013) used 69 RQ AGN in the COSMOS and ECDFS fields at $z < 2$ and found a significant correlation between the X-ray spectral index and n_{Edd} . However, based on their analysis, the scatter of the $\Gamma - n_{\text{Edd}}$ relation is large, and thus the relation is only suitable for large samples and not for individual sources. We note, though, that the L_{bol} of their sources was calculated following a mix of different methods (SED fitting and bolometric correction to the L_{X}), and this may contribute to the scatter. Trakhtenbrot et al. (2017) used 228 hard X-ray-selected AGN from the *Swift*/Bat AGN Spectroscopic Survey (BASS) and found a very weak but statistically significant correlation between Γ and n_{Edd} . Nonetheless, their M_{BH} measurements come from several different methods (see their Sect. 2.3), and they reported that the correlation was weaker or even absent within their different subsets. More recently, Kamraj et al. (2022) used 195 Seyfert 1 AGN in the local Universe ($z < 0.2$) with *NuSTAR* and *Swift*/XRT or XMM observations. They studied the correlation between the X-ray spectral index and n_{Edd} using three models to fit the X-ray spectra of their sources. They found considerable scatter and no strong trend between Γ and n_{Edd} for all the spectral models they applied. They concluded that the $\Gamma - n_{\text{Edd}}$ may not be universal nor robust and could vary with the choice of the sample, the luminosity range probed, and the energy range of X-ray data used in the analysis. We note that their M_{BH} estimates come from the second data release of the optical measurements from the BASS survey and were inferred using a compilation of different techniques (e.g. broad-line measurements from optical spectra, stellar velocity dispersions, reverberation mapping), which could increase the scatter in the $\Gamma - n_{\text{Edd}}$ and weaken any possible correlation.

Combining the results of our analysis with those from previous works, we conclude that caution has to be taken when compiling results from different studies that have used different methods to measure the M_{BH} and the L_{bol} . Furthermore, the correlation between Γ and n_{Edd} may not be universal and could (also) depend on the level of the X-ray obscuration of the sources.

6. Conclusions

The parent sample of this work includes $\sim 35\,000$ X-ray AGN included in the 4XMM-DR11 catalogue for which there are available X-ray spectra fitting measurements. To measure the host galaxy properties of these sources, we matched them with multiwavelength datasets and constructed their SEDs. Using the CIGALE SED fitting algorithm, we calculated the SFR and M_* of the AGN. Our analysis demanded stringent selection criteria to ensure that only AGN with dependable X-ray spectral and

SED fitting measurements were incorporated in our investigation. There were 1443 AGN that fulfilled these requirements. We then applied strict criteria using the N_{H} values and their associated uncertainties to classify sources into obscured and unobscured AGN and compared their SMBH and host galaxy properties. Our main findings are the following:

- Obscured AGN tend to live in more massive systems (by ~ 0.1 dex) compared to unobscured AGN. The difference, although small, appears to be statistically significant. Obscured sources also tend to live in galaxies with a lower SFR (by ~ 0.25 dex) compared to their unobscured counterparts; however, this difference is not statistically significant. The results do not depend on the N_{H} threshold used to classify AGN ($N_{\text{H}} = 10^{23} \text{ cm}^{-2}$ or $N_{\text{H}} = 10^{22} \text{ cm}^{-2}$), and the differences are not statistically significant at high L_{X} ($\log [L_{\text{X}}(\text{ergs}^{-1})] > 44$) nor if we disregard the errors associated with the N_{H} measurements.
- Unobscured AGN have, on average, higher specific black hole accretion rates (a proxy of the Eddington ratio) compared to unobscured sources. The difference is 0.1–0.2 dex and appears to have a high statistical significance.

Furthermore, we cross-matched our dataset with the catalogue of Wu & Shen (2022), which includes measurements for the M_{BH} , L_{bol} , and Eddington ratio, among others, for $\sim 750\,000$ QSOs from SDSS. There are 271 type 1 AGN in common between the two datasets up to a redshift of 1.9. We studied the n_{Edd} and M_{BH}/M_* ratio of the two AGN populations, and we examined if there is a correlation between Γ and n_{Edd} . Our main results are summarised as follows:

- Type 1 AGN with $N_{\text{H}} > 10^{22} \text{ cm}^{-2}$ tend to have a higher M_{BH} compared to type 1 sources with lower N_{H} values at similar M_* .
- For type 1 AGN, the M_{BH}/M_* ratio is nearly constant, with N_{H} up to $N_{\text{H}} = 10^{22} \text{ cm}^{-2}$. However, our results suggest that the M_{BH}/M_* ratio increases at higher N_{H} values.
- A correlation was found between the spectral photon index, Γ , and the Eddington ratio, n_{Edd} , for type 1 AGN with $N_{\text{H}} < 10^{22} \text{ cm}^{-2}$.

The findings of our work indicate that the inconsistent results among previous studies regarding the host galaxy properties of obscured and unobscured AGN could mainly be due to the different luminosities probed. Additionally, our analysis indicates that during the obscured phase, SMBH growth exceeds that of the host galaxies, potentially implying a sequential growth pattern where M_{BH} develops first, while early stellar mass assembly might not be as efficient. Furthermore, the disparities in previous research regarding the correlation between Γ and n_{Edd} may also be partly attributed to differences in the fraction of obscured and unobscured AGN within the samples used in those studies.

Acknowledgements. This project has received funding from the European Union's Horizon 2020 research and innovation program under grant agreement no. 101004168, the XMM2ATHENA project. This research has made use of data obtained from the 4XMM *XMM-Newton* serendipitous source catalogue compiled by the 10 institutes of the *XMM-Newton* Survey Science Centre selected by ESA. Funding for the Sloan Digital Sky Survey V has been provided by the Alfred P. Sloan Foundation, the Heising-Simons Foundation, the National Science Foundation, and the Participating Institutions. SDSS acknowledges support and resources from the Center for High-Performance Computing at the University of Utah. The SDSS web site is www.sdss.org. SDSS is managed by the Astrophysical Research Consortium for the Participating Institutions of the SDSS Collaboration, including the Carnegie Institution for Science, Chilean National Time Allocation Committee (CNTAC) ratified researchers, the Gotham Participation Group, Harvard University, Heidelberg University, The Johns Hopkins University, L'École polytechnique fédérale de Lausanne (EPFL), Leibniz-Institut für Astrophysik Potsdam (AIP), Max-Planck-Institut

fur Astronomie (MPIA Heidelberg), Max-Planck-Institut für Extraterrestrische Physik (MPE), Nanjing University, National Astronomical Observatories of China (NAOC), New Mexico State University, The Ohio State University, Pennsylvania State University, Smithsonian Astrophysical Observatory, Space Telescope Science Institute (STScI), the Stellar Astrophysics Participation Group, Universidad Nacional Autónoma de México, University of Arizona, University of Colorado Boulder, University of Illinois at Urbana-Champaign, University of Toronto, University of Utah, University of Virginia, Yale University, and Yunnan University. The Pan-STARRS1 Surveys (PS1) and the PS1 public science archive have been made possible through contributions by the Institute for Astronomy, the University of Hawaii, the Pan-STARRS Project Office, the Max-Planck Society and its participating institutes, the Max Planck Institute for Astronomy, Heidelberg and the Max Planck Institute for Extraterrestrial Physics, Garching, The Johns Hopkins University, Durham University, the University of Edinburgh, the Queen's University Belfast, the Harvard-Smithsonian Center for Astrophysics, the Las Cumbres Observatory Global Telescope Network Incorporated, the National Central University of Taiwan, the Space Telescope Science Institute, the National Aeronautics and Space Administration under Grant No. NNX08AR22G issued through the Planetary Science Division of the NASA Science Mission Directorate, the National Science Foundation Grant No. AST-1238877, the University of Maryland, Eotvos Lorand University (ELTE), the Los Alamos National Laboratory, and the Gordon and Betty Moore Foundation. This publication makes use of data products from the Wide-field Infrared Survey Explorer, which is a joint project of the University of California, Los Angeles, and the Jet Propulsion Laboratory/California Institute of Technology, funded by the National Aeronautics and Space Administration. This research has made use of TOPCAT version 4.8 (Taylor 2005) and Astropy (Astropy Collaboration 2022).

References

- Aird, J., Coil, A. L., & Georgakakis, A. 2018, *MNRAS*, **474**, 1225
- Arnaud, K. A. 1996, *ASP Conf. Ser.*, **101**, 17
- Astropy Collaboration (Price-Whelan, A. M., et al.) 2022, *ApJ*, **935**, 167
- Bolton, A. S., Schlegel, D. J., Aubourg, É., et al. 2012, *AJ*, **144**, 144
- Boquien, M., Burgarella, D., Roehlly, Y., et al. 2019, *A&A*, **622**, A103
- Boyle, B. J., Shanks, T., Croom, S. M., et al. 2000, *MNRAS*, **317**, 1014
- Brightman, M., Silverman, J. D., Mainieri, V., et al. 2013, *MNRAS*, **433**, 2485
- Bruzual, G., & Charlot, S. 2003, *MNRAS*, **344**, 1000
- Buat, V., Ciesla, L., Boquien, M., Malek, K., & Burgarella, D. 2019, *A&A*, **632**, A79
- Buat, V., Mountrichas, G., Yang, G., et al. 2021, *A&A*, **654**, A93
- Buchner, J. 2019, *PASP*, **131**, 108005
- Buchner, J., Georgakakis, A., Nandra, K., et al. 2014, *A&A*, **564**, A125
- Buchner, J., Brightman, M., Balokovic, M., et al. 2021, *A&A*, **651**, A58
- Chabrier, G. 2003, *PASP*, **115**, 763
- Charlot, S., & Fall, S. M. 2000, *ApJ*, **539**, 718
- Ciotti, L., & Ostriker, J. P. 1997, *ApJ*, **487**, L105
- Dale, D. A., Helou, G., Magdis, G. E., et al. 2014, *ApJ*, **784**, 83
- Davis, S. W., & Laor, A. 2011, *ApJ*, **728**, 98
- Esparza-Arredondo, D., Gonzalez-Martín, O., Dultzin, D., et al. 2021, *A&A*, **651**, A91
- Evans, P. A., Page, K. L., Osborne, J. P., et al. 2020, *ApJS*, **247**, 54
- Ferrarese, L., & Merritt, D. 2000, *ApJ*, **539**, 9
- Georgakakis, A., Aird, J., Schulze, A., et al. 2017, *MNRAS*, **471**, 1976
- Georgantopoulos, I., Poulidas, E., Mountrichas, G., et al. 2023, *A&A*, **673**, A67
- Häring, N., & Rix, H.-W. 2004, *ApJ*, **604**, L89
- Hopkins, P. F., Hernquist, L., Cox, T. J., et al. 2006, *ApJS*, **163**, 1
- Kamraj, N., Balokovic, M., Brightman, M., et al. 2019, *ApJ*, **887**, 255
- Kamraj, N., Brightman, M., Harrison, F. A., et al. 2022, *ApJ*, **927**, 42
- Kelly, B. C. 2007, *ApJ*, **665**, 1489
- Koutoulidis, L., Mountrichas, G., Georgantopoulos, I., Poulidas, E., & Plionis, M. 2022, *A&A*, **658**, A35
- Lanzuisi, G., Delvecchio, I., Berta, S., et al. 2017, *A&A*, **602**, A123
- Lopez, I. E., Brusa, M., Bonoli, S., et al. 2023, *A&A*, **672**, A137
- Lusso, E., Comastri, A., Simmons, B. D., et al. 2012, *MNRAS*, **425**, 623
- Lyke, B. W., Higley, A. N., McLane, J. N., et al. 2020, *ApJS*, **250**, 8
- Magorrian, J., Tremaine, S., Richstone, D., et al. 1998, *AJ*, **115**, 2285
- Malek, K., Buat, V., Roehlly, Y., et al. 2018, *A&A*, **620**, A50
- Marinucci, A., Bianchi, S., Matt, G., et al. 2016, *MNRAS*, **456**, L94
- Masoura, V. A., Mountrichas, G., Georgantopoulos, I., et al. 2018, *A&A*, **618**, A31
- Masoura, V. A., Georgantopoulos, I., Mountrichas, G., et al. 2020, *A&A*, **638**, A45
- Masoura, V. A., Mountrichas, G., Georgantopoulos, I., & Plionis, M. 2021, *A&A*, **646**, A167
- Mateos, S., Barcons, X., Carrera, F. J., et al. 2005, *A&A*, **444**, 79
- Mateos, S., Carrera, F. J., Page, M. J., et al. 2010, *A&A*, **510**, A35
- Merloni, A., Bongiorno, A., Brusa, M., et al. 2014, *MNRAS*, **437**, 3550
- Mountrichas, G. 2023, *A&A*, **672**, A98
- Mountrichas, G., & Buat, V. 2023, *A&A*, **679**, A151
- Mountrichas, G., & Shankar, F. 2023, *MNRAS*, **518**, 2088
- Mountrichas, G., Georgakakis, A., & Georgantopoulos, I. 2019, *MNRAS*, **483**, 1374
- Mountrichas, G., Buat, V., Georgantopoulos, I., et al. 2021a, *A&A*, **653**, A70
- Mountrichas, G., Buat, V., Yang, G., et al. 2021b, *A&A*, **646**, A29
- Mountrichas, G., Buat, V., Yang, G., et al. 2021c, *A&A*, **653**, A74
- Mountrichas, G., Buat, V., Yang, G., et al. 2022a, *A&A*, **663**, A130
- Mountrichas, G., Buat, V., Yang, G., et al. 2022b, *A&A*, **667**, A145
- Mountrichas, G., Masoura, V. A., Xilouris, E. M., et al. 2022c, *A&A*, **661**, A108
- Mountrichas, G., Yang, G., Buat, V., et al. 2023, *A&A*, **675**, A137
- Nenkova, M., Ivezić, Ž., & Elitzur, M. 2002, *ApJ*, **570**, L9
- Netzer, H. 2015, *ARA&A*, **53**, 365
- Ogawa, S., Ueda, Y., Tanimoto, A., & Yamada, S. 2021, *ApJ*, **906**, 84
- Poulidas, E., Mountrichas, G., Georgantopoulos, I., et al. 2022, *A&A*, **667**, A56
- Ricci, C., Ho, L. C., Fabian, A. C., et al. 2018, *MNRAS*, **480**, 1819
- Risaliti, G., Young, M., & Elvis, M. 2009, *ApJ*, **700**, L6
- Ruiz, A., Corral, A., Mountrichas, G., & Georgantopoulos, I. 2018, *A&A*, **618**, A52
- Sarria, J. E., Maiolino, R., Franca, F. L., et al. 2010, *A&A*, **522**, L3
- Scott, A. E., Stewart, G. C., Mateos, S., et al. 2011, *MNRAS*, **417**, 992
- Shemmer, O., Brandt, W. N., Netzer, H., Maiolino, R., & Kaspi, S. 2008, *ApJ*, **682**, 81
- Shimizu, T. T., Davies, R. I., Koss, M., et al. 2018, *ApJ*, **856**, 154
- Sobolewska, M. A., & Papadakis, I. E. 2009, *MNRAS*, **399**, 1597
- Sobral, D., Smail, I., Best, P. N., et al. 2013, *MNRAS*, **428**, 1128
- Somerville, R. S., Hopkins, P. F., Cox, T. J., Robertson, B. E., & Hernquist, L. 2008, *MNRAS*, **391**, 481
- Stalewski, M., Fritz, J., Baes, M., Nakos, T., & Popović, L. Č. 2012, *MNRAS*, **420**, 2756
- Stalewski, M., Ricci, C., Ueda, Y., et al. 2016, *MNRAS*, **458**, 2288
- Suh, H., Civano, F., Trakhtenbrot, B., et al. 2020, *ApJ*, **889**, 32
- Sun, M., Trump, J. R., Brandt, W. N., et al. 2015, *ApJ*, **802**, 14
- Taylor, M. B. 2005, in *Astronomical Data Analysis Software and Systems XIV*, eds. P. Shopbell, M. Britton, & R. Ebert, *ASP Conf. Ser.*, **347**, 29
- Trakhtenbrot, B., Ricci, C., Koss, M. J., et al. 2017, *MNRAS*, **470**, 800
- Tranin, H., Godet, O., Webb, N., & Primorac, D. 2022, *A&A*, **657**, A138
- Tristram, K. R. W., Meisenheimer, K., Jaffe, W., et al. 2007, *A&A*, **474**, 837
- Trump, J. R., Impey, C. D., Elvis, M., et al. 2009, *ApJ*, **696**, 1195
- Urry, C. M., & Padovani, P. 1995, *PASP*, **107**, 803
- Vasudevan, R. V., & Fabian, A. C. 2007, *MNRAS*, **381**, 1235
- Villa-Velez, J. A., Buat, V., Theule, P., Boquien, M., & Burgarella, D. 2021, *A&A*, **654**, A153
- Webb, N. A., Coriat, M., Traulsen, I., et al. 2020, *A&A*, **641**, A136
- Webb, N. A., Carrera, F. J., Schwobe, A., et al. 2023, *Astron. Nachr.*, **344**, e20220102
- Wu, Q., & Shen, Y. 2022, *ApJS*, **263**, 42
- Yang, G., Boquien, M., Buat, V., et al. 2020, *MNRAS*, **491**, 740
- Yang, G., Boquien, M., Brandt, W. N., et al. 2022, *ApJ*, **927**, 192
- Zou, F., Yang, G., Brandt, W. N., & Xue, Y. 2019, *ApJ*, **878**, 11